MATERIALS CHEMISTRY
FRONTIERS

RESEARCH ARTICLE

View Article Online
View Journal | View Issue

Cite this: *Mater. Chem. Front.*, 2020, **4**, 3074

Nanosilver-enhanced AIE photosensitizer for simultaneous bioimaging and photodynamic therapy†

Mohammad Tavakkoli Yaraki,[ab] Yutong Pan,‡[b] Fang Hu,‡[bc] Yong Yu,[a] Bin Liu *[b] and Yen Nee Tan *[ad]

Theranostic photosensitizers which enable both disease diagnosis and effective treatment have recently received much attention towards personalized medicine. Herein, we report a multifunctional nanohybrid system using silver nanoparticles (AgNPs) to enhance the singlet oxygen generation (SOG) and fluorescence properties of a unique photosensitizer with aggregation-induced emission (AIE-PS) for simultaneous bioimaging and photodynamic therapy. To study the metal-enhancement effects, 4-mercaptobenzoic acid-capped AgNPs with well-controlled size (14, 40, and 80 nm) were synthesized to form nanohybrids with a specially designed red-emissive AIE-PS *via* simple electrostatic interactions. The careful control of the Ag nanoparticle concentration and the unique design of 80 nm AgNP@red-emissive AIE in this study resulted in a 10-fold enhancement in SOG, which is higher than other reported ME-SOG systems using similar plasmonic enhancers. Furthermore, the as-developed AgNP@AIE-PS nanohybrid exhibited improved photostability with negligible fluorescence quenching (5%), which is important for cell tracking. In addition, cytotoxity tests showed that these nanohybrids are biocompatibile with normal NIH-3T3 cells under dark conditions. Thus, they were employed for simultaneous imaging and photodynamic ablation of HeLa cancer cells. The results show that this brightly fluorescent AgNP@AIE-PS enabled about 4 times higher efficacy in PDT as compared to the control sample (*i.e.*, 85% *vs.* 20% cell death) under low intensity white light irradiation (40 mW cm^{-2}) for only 10 minutes, demonstrating its promising potential for advanced theranostic treatment in future nanomedicine.

Received 9th July 2020,
Accepted 10th August 2020

DOI: 10.1039/d0qm00469c

rsc.li/frontiers-materials

1. Introduction

Developing multifunctional hybrid nanomaterials for simultaneous diagnosis and effective cancer treatment *via* fluorescence imaging and photodynamic therapy has received much interest in recent years.[1–7] Photodynamic therapy (PDT) is an emerging non-invasive technique based on the use of light, oxygen, and photosensitizing molecules to produce reactive oxygen species (ROS) for killing cancer and/or bacterial cells.[8–12] In particular, efficient PDT relies on the generation of sufficient ROS, especially singlet oxygen ($^1O_2$), to be able to disrupt the 'stubborn' microbial and cancerous cells.[13–15] Although some of the conventional photosensitizers are also fluorescent molecules, most of them are not soluble in water, making them easily aggregate at high concentrations in the biological medium due to π–π stacking.[16] This often leads to reduced singlet oxygen generation abilities and also reduced fluorescence due to the self-quenching effect.[3,17–19] Therefore, there is a pressing need to develop new generation PDT agents that could overcome the drawbacks of traditional photosensitizers for effective theranostic treatment.

Nowadays, aggregation-induced emission photosensitizers (AIE-PSs) have received much attention in the biomedicine communities owing to their intrinsic fluorescence which could be "turned on" in the aggregate state for disease monitoring while generating singlet oxygen species for PDT treatment.[17,20–22] For biological applications,[23] water-soluble AIE molecules or AIE-PSs can be easily designed by introducing charged moieties

---

[a] Institute of Materials Research and Engineering, Agency for Science, Technology and Research (A*STAR), 138634, Singapore

[b] Department of Chemical and Biomolecular Engineering, National University of Singapore, 4 Engineering Drive 4, Singapore 117585, Singapore. E-mail: cheliub@nus.edu.sg

[c] Guangdong Provincial Key Laboratory of Construction and Detection in Tissue Engineering, Biomaterials Research Center, School of Biomedical Engineering, Southern Medical University, Guangzhou 510515, China

[d] Faculty of Science, Agriculture & Engineering, Newcastle University, Newcastle Upon Tyne NE1 7RU, UK. E-mail: yennee.tan@newcastle.ac.uk

† Electronic supplementary information (ESI) available. See DOI: 10.1039/d0qm00469c

‡ Y. P. and F. H. contributed equally to this work.

onto the AIE-cores, such as tetraphenylethene (TPE) and tetraphenylsilole (TPS). As such, the aggregation-induced properties of AIE-PSs can also be enhanced by interacting with oppositely charged molecules or metal nanoparticles to form an 'enhanced' hybrid system for effective theranostic treatment. Furthermore, as most AIE-PSs have greater photostability and resistance to chemical degradation as compared to the conventional fluorophores or photosensitizers, they are more suitable for use in long term cancer cell tracking and treatment when they are irradiated under white light for an extended period of time. All these unique features of AIE-PSs make them a promising candidate for use in next generation PDT.[24–27]

Other than exploring new designs of photosensitizers, a plasmonic enhancement strategy has been exploited to improve their singlet oxygen generation efficiency,[28,29] termed metal-enhanced singlet oxygen generation (ME-SOG). Similar to the theory of metal-enhanced fluorescence (MEF)[30–32] and surface-enhanced Raman scattering,[33–35] there are many factors affecting ME-SOG, including the size[36,37] and shape[34,38] of the metal nanoparticles (NPs) as well as the distance between the photosensitizer (PS) and the metal NPs.[37–39] Typically, the photosensitizer can be either directly in contact with the metal surface[29,36,40–42] or separated by a dielectric spacer[38,39] to balance the competition between the enhanced excitation rate and non-radiative energy transfer from the excited PS* molecule to the metal surface. However, to the best of our knowledge, metal-enhanced singlet oxygen generation of AIE-PSs has not been systematically studied or designed for theranostic applications.

It is well known that photosensitization and fluorescence are competing processes for any photosensitizer, which makes it very difficult to enhance the photosensitization without affecting the fluorescence. Herein, we report a multifunctional silver nanoparticle-AIE photosensitizer (AgNP@AIE-PS) hybrid system to enhance the singlet oxygen generation efficiency of the AIE-PS without affecting its fluorescence brightness *via* systematic plasmonic engineering. Specifically, negatively charged 4-mercaptobenzoic acid-capped AgNPs and positively charged red-emissive AIE-PSs were used to form AgNP@AIE-PS through a simple electrostatic-induced aggregation approach. The SOG efficiency of the hybrid system was examined by a chemical trapping method while the photophysical properties were characterized using various techniques such as UV-visible (UV-vis) and photoluminescence spectroscopy, transmission electron microscopy (TEM) and time-resolved fluorescence spectroscopy. The plasmonic enhancement effects in SOG were assessed by comparing it with a control sample made from AIE-PS loaded silica nanoparticles (SNP@AIE-PS). The results show that a maximum 10-fold enhancement in singlet oxygen generation with minimum fluorescence quenching (~5%) could be achieved for the 80 nm AgNP@AIE-PS. It was also found that the as-developed 80 nm AgNP@AIE-PS possesses high photostability in the hybrid system with good biocompatibility, and it has been applied successfully for simultaneous bioimaging and photodynamic therapy in cancer cell ablation as demonstrated in this study.

2. Results and discussion

2.1. Metal-enhanced singlet oxygen generation of the AIE-PS

The theranostic PS used in this study was synthesized from an AIE molecule with a tetraphenylethylene backbone modified with vinyl pyridinium[43] (Fig. 1a). The as-synthesized AIE-PS is red-emissive when aggregated in a weak solvent, *e.g.*, phosphate buffer solution. It shows a maximum absorption peak at 400 nm from the UV-vis absorption spectrum and an emission peak at 625 nm (Fig. 1b). The fluorescence quantum yield of the aggregated AIE-PS was measured to be 1.8% using 4-(dicyanomethylene)-2-methyl-6-(*p*-dimethylaminostyryl)-4*H*-pyran (DCM) as a reference.[43] The singlet oxygen ($^1O_2$) generation property of the red-emissive AIE-PS was studied by a chemical trapping method using 9,10-anthracenediyl-bis(methylene)dimalonic acid (ABDA) as the probe, where a decrease in the absorption peak of ABDA corresponds to the amount of $^1O_2$ reacted. As shown in Fig. 1c, the as-synthesized AIE-PS also possesses good $^1O_2$ generation as evidenced by the rapid decrease of the ABDA characteristic peaks (*i.e.*, about 65% of ABDA was degraded in 20 min upon white light irradiation). The $^1O_2$ quantum yield of the red-emissive AIE-PS was estimated to be 78.5% as compared to the conventional photosensitizer Rose Bengal (75%) using ABDA as the $^1O_2$ trapping agent (Fig. S1, ESI†). The good photosensitization ability of the AIE-PS is due to the introduction of electron donor and electron acceptor groups onto the TPE molecule, which decreases the singlet–triplet energy (Δ_{ST}), leading to an increase in the intersystem crossing (ISC) rate and better singlet oxygen generation efficiency relative to that of TPE.[44]

For the study of metal-enhanced singlet oxygen generation, three distinct sizes of silver nanoparticles (AgNPs) capped with 4-mercaptobenzoic acid were synthesized (Fig. 1c). The size and zeta potential of the as-prepared 4-MBA-capped AgNPs were measured using transmission electron microscopy (TEM) and a Zetasizer, respectively. As shown in Fig. 1d–f, three samples of the 4-MBA-capped AgNPs showed a uniform distribution of particle sizes with a mean diameter of 14 ± 3 (14 nm AgNPs), 40 ± 9 nm (40 nm AgNPs) and 80 ± 13 nm (80 nm AgNPs), respectively. These negatively charged AgNPs (see the respective zeta potential values in Fig. S2, ESI†) were then mixed with the positively charged AIE-PS in aqueous solution (pH = 4) to prepare the AgNP@AIE-PS hybrid systems *via* electrostatic attraction forces (see the Experimental section for details).

The singlet oxygen generation rate of AgNP@AIE-PS could be monitored using ABDA as the $^1O_2$ trapping probe, and was determined by the first-order kinetic constant (K_{ABDA}) of ABDA's degradation rate. That is, the larger K_{ABDA}, the faster the $^1O_2$ generation of the sample. Fig. 2a shows the $^1O_2$ generation of AgNP@AIE-PS prepared with the AgNPs of different sizes (*i.e.*, 14 nm, 50 nm, and 80 nm) at varied concentrations. It was observed that the $^1O_2$ generation rate of AgNP@AIE-PS increases as more AgNPs were introduced until it reaches a maximum value at its optimum concentration, beyond which the $^1O_2$ generation rate decreases. The optimum concentrations of AgNPs to achieve maximum $^1O_2$ generation as indicated by the first-order kinetic constant were 3 pM for 14 nm AgNPs (K_{ABDA} = 0.0682 min^{-1}), 2 pM for 50 nm AgNPs (K_{ABDA} = 0.0721 min^{-1})

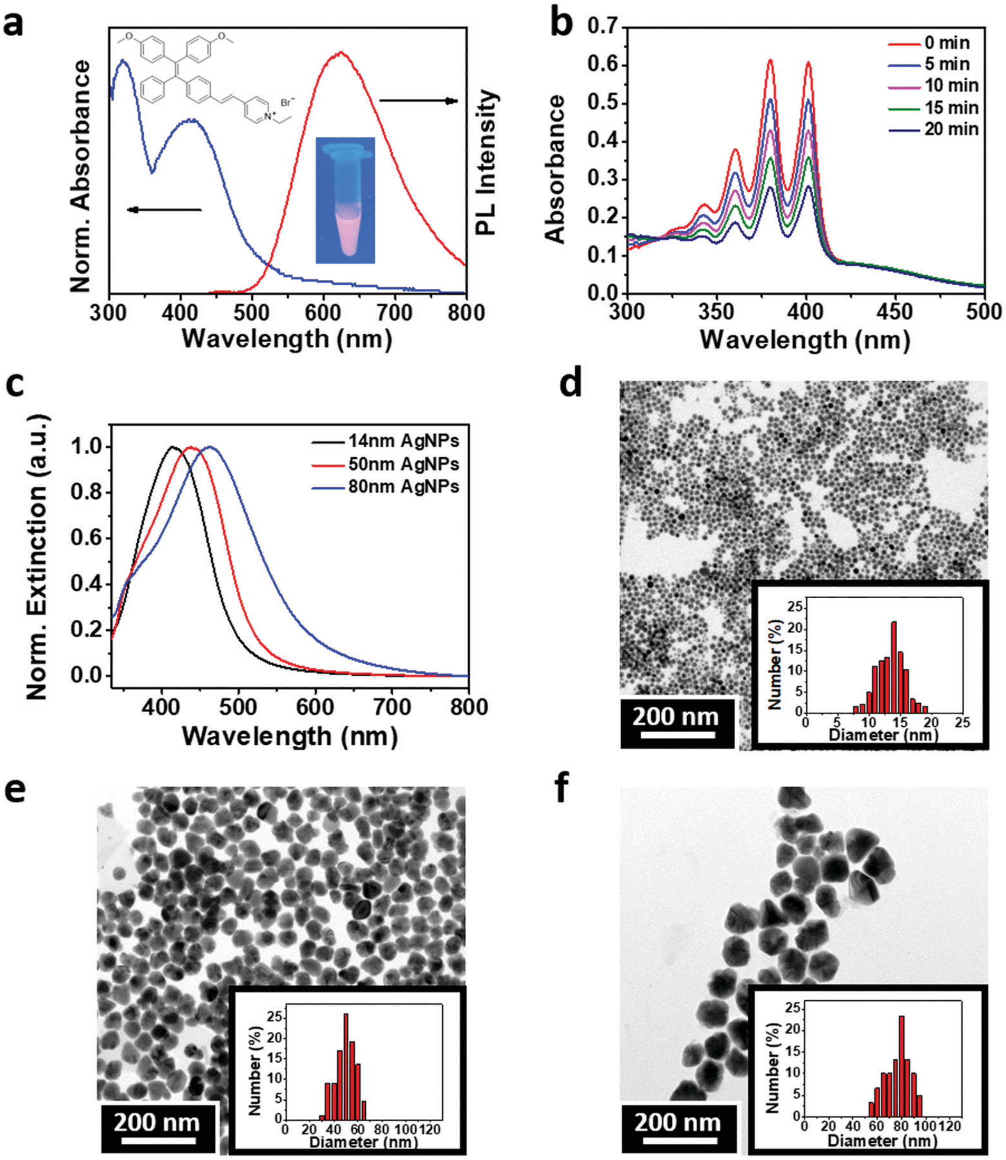

Fig. 1 (a) UV-vis (blue line, left axis) and fluorescence spectra (red line, right axis) of the AIE-PS. The insets show the molecular structure and fluorescence image of the AIE-PS molecule in PBS buffer under UV light. (b) Time profile showing the absorption spectra of ABDA (50 μM) in the presence of the AIE-PS (9 μM) under 40 mW cm^{-2} white light irradiation. (c) Normalized extinction spectra, and TEM images of 4-MBA-capped AgNPs with three distinct sizes: (d) 14 nm AgNPs (14 ± 2.7 nm), (e) 50 nm AgNPs (50 ± 8.9 nm), and (f) 80 nm AgNPs (80 ± 12.7 nm). The insets show the size distribution of the obtained AgNPs.

and 0.22 pM for 80 nm AgNPs (K_{ABDA} = 0.1831 min^{-1}). Interestingly, the addition of much fewer 80 nm AgNPs led to the highest $^1O_2$ generation among the tested AgNPs of different sizes. This could be attributed to the relationship between the plasmonic effect of the Ag NPs and their surface coverage by the AIE-PS molecules. Hence, the maximum $^1O_2$ generation rate is expected to be observed for the samples with maximum surface coverage, where a further increase in the concentration of AgNPs could lead to a lesser number of AIE-PS molecules deposited on the surface of the AgNPs. To examine this hypothesis, the amounts of adsorbed AIE-PS molecules on the three samples of AgNP@AIE-PS with maximum $^1O_2$ generation rate at their optimum concentration (*i.e.*, 3, 2, and 0.22 pM for 14 nm AgNPs, 50 nm AgNPs, and 80 nm AgNPs, respectively) were determined experimentally. Specifically, AgNP@AIE-PS (before addition of PBS) was centrifuged to obtain the supernatant, where its absorbance intensity was measured and compared with that in the initial AIE-PS solution (9 μM).

For the control sample, the same amount of AIE-PS molecules was loaded onto negatively-charged silica nanoparticles (SNP) with a diameter of 104 ± 3 nm and zeta potential of −29.6 ± 1 mV.[33] As such, AIE-PS molecules on the surface of SNP would adsorb in the same aggregation state as that on the surface of AgNPs. Hence, the SOG enhancement factor (EF_{SOG}) of AgNP@AIE-PS can be calculated based on the first-order kinetic constant of ABDA degradation in the presence of the

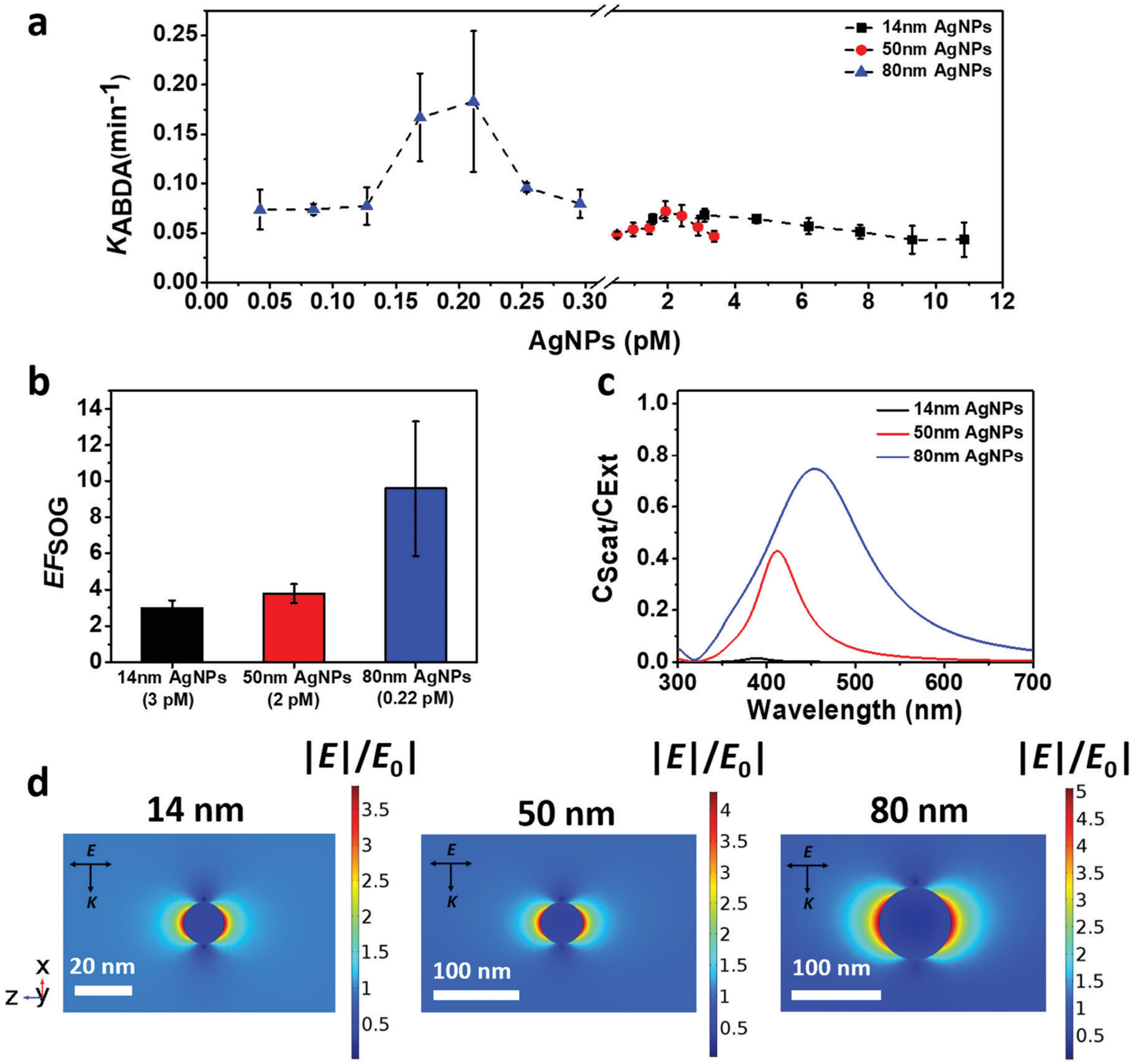

Fig. 2 (a) Plot of the ABDA kinetic constant (K_{ABDA}) *vs.* different concentrations of AgNPs showing the plasmonic enhancement effect of 14 nm AgNPs (squares), 50 nm AgNPs (spheres), and 80 nm AgNPs (triangles) on the singlet oxygen generation efficiency of the AIE-PS; (b) calculated SOG enhancement factor ($\mathrm{EF_{SOG}}$) for AgNP@AIE-PS at the respective optimum concentration of AgNPs; and simulated (c) scattering contribution ($C_{\mathrm{Scat}}/C_{\mathrm{Ext}}$) and (d) electric field distribution of AgNPs in water, where C_{Scat} and C_{Ext} are the scattering and extinction efficiency of the AgNPs, respectively. The arrows for *E* and *K* indicate the direction of electric field polarization and incident light propagation, respectively.

metal-enhanced sample ($K_{\mathrm{AgNP@AIE-PS}}$) and control sample ($K_{\mathrm{SNP@AIE-PS}}$), respectively, using the following equation:

$$\mathrm{EF_{SOG}} = \frac{K_{\mathrm{AgNP@AIE-PS}}}{K_{\mathrm{SNP@AIE-PS}}} \tag{1}$$

Fig. 2b shows the SOG enhancement factor as a function of AgNP size in the order of 14 nm AgNPs < 50 nm AgNPs < 80 nm AgNPs, where a maximum ~10-fold enhancement was observed for the 80 nm AgNP@AIE-PS sample. This trend is consistent with the size-dependent light scattering contribution ($C_{\mathrm{Scat}}/C_{\mathrm{Ext}}$) of AgNPs in Fig. 2c, which was obtained by the mathematical simulations of absorbance, scattering and extinction spectra of individual AgNPs (Fig. S3, ESI†). The size-dependency of ME-SOG as observed is due to the plasmonic coupling between the AgNPs and excited AIE-PS molecules where larger metal nanoparticles are known to exhibit stronger field enhancement than that of the smaller ones.[36,45] The simulation results in Fig. 2d further show that the electric field surrounding the surface of the 80 nm AgNPs is stronger as compared with the respective 50 nm AgNPs and 14 nm AgNPs under a plane-wave light source with a wavelength of 625 nm (*i.e.*, the maximum emission wavelength of the AIE-PS).

2.2. Plasmonic effects on the photophysical properties of AgNP@AIE-PS

To assess the plasmonic effect of the AgNPs on the fluorescence properties of the red-emissive AIE-PS, the photoluminescent intensity (PL) of the AgNP@AIE-PS samples was measured (Fig. S4, ESI†) and used to calculate the fluorescence quantum yield (see the ESI,† SI-S3, for detailed calculations). It was found that the presence of AgNPs quenched the fluorescence of the

AIE-PS in the hybrid system. Fig. 3a shows the change in the fluorescence quantum yield of AgNP@AIE-PS with different AgNP concentrations. Unlike other particle sizes across different concentrations, there is only a slight change in the fluorescence quantum yield of the AIE-PS when it was adsorbed onto the surface of 80 nm AgNPs ($<$10% for all tested concentrations). To further evaluate the fluorescence quenching mechanism of AgNP@AIE-PS, the spectral overlap ($J(\lambda)$) between the extinction of AgNPs (as the acceptor) and emission of the AIE-PS (as the donor), as shown in Fig. 3b, was quantified using the following equation:

$$J(\lambda) = \int_0^{\lambda} F(\lambda)\varepsilon(\lambda)\lambda^4 \mathrm{d}\lambda \qquad (2)$$

where $F(\lambda)$ is the normalized fluorescence spectrum of the AIE-PS and $\varepsilon(\lambda)$ is the molar extinction coefficient of the AgNPs in mol^{-1} dm^3 cm^{-1} at a certain wavelength (λ). The calculated values of $J(\lambda)$ for the different sizes of AgNPs are 2.96×10^{-13} for the 14 nm AgNPs, 4.63×10^{-13} for the 50 nm AgNPs and 2.29×10^{-12} for the 80 nm AgNPs, which are considerably less than those obtained for the reported fluorescence energy transfer (FRET) pairs.[46,47] Thus, non-radiative energy transfer from the AIE-PS to AgNPs *via* other mechanisms than FRET is expected (Fig. 3c). Despite the fact that few mechanisms[48,49] have been proposed to explain the energy transfer between a donor and acceptor pair, nanometal surface energy transfer (NSET) is the one providing a better correlation between the theory and experimental fluorescence quenching results when the fluorescence of a fluorophore is quenched in the vicinity of a metallic surface with insufficient spectral overlap.[50] As can be seen in Fig. 3d, NSET is the main responsible mechanism for the fluorescence quenching as observed in AgNP@AIE-PS (see the ESI,† SI-5, for detailed calculations).

Next, the photophysical properties of the red-emissive AgNP@AIE-PS hybrids with the greatest SOG enhancement factor at each particle size were investigated (Fig. 2a). Fig. 4a shows that the fluorescence lifetime of AIE-PS molecules in the hybrid system decreases when they were attached to the surface of AgNPs. It is noticed that the presence of larger AgNPs (*e.g.*, 80 *vs.* 14 nm) would lead to a shorter fluorescence lifetime (*i.e.*, 4.25 *versus* 4.64 ns) as observed in the AgNP@AIE-PS studied herein. However, there is no direct correlation between the energy transfer efficiency of the hybrids (*i.e.*, 9% for 14 nm AgNP@AIE-PS, 32% for 50 nm AgNP@AIE-PS, and 5% for 80 nm AgNP@AIE-PS) and their fluorescence lifetime. This could be explained by the modification of both radiative and non-radiative decay rates in the vicinity of AgNPs due to the enhanced electric field around them.[32,51] As shown in Fig. 4b, the net absorbance spectra of the AIE-PS have been increased in the presence of AgNPs of increasing sizes. This provides strong evidence to support the observation that the 80 nm AgNP@AIE-PS exhibited the highest SOG enhancement factor among other nanohybrids with smaller particle sizes. In addition, the presence of plasmonic NPs also enhanced the photostability of 80 nm AgNP@AIE-PS as compared with the AIE-PS alone in PBS (Fig. 4c),

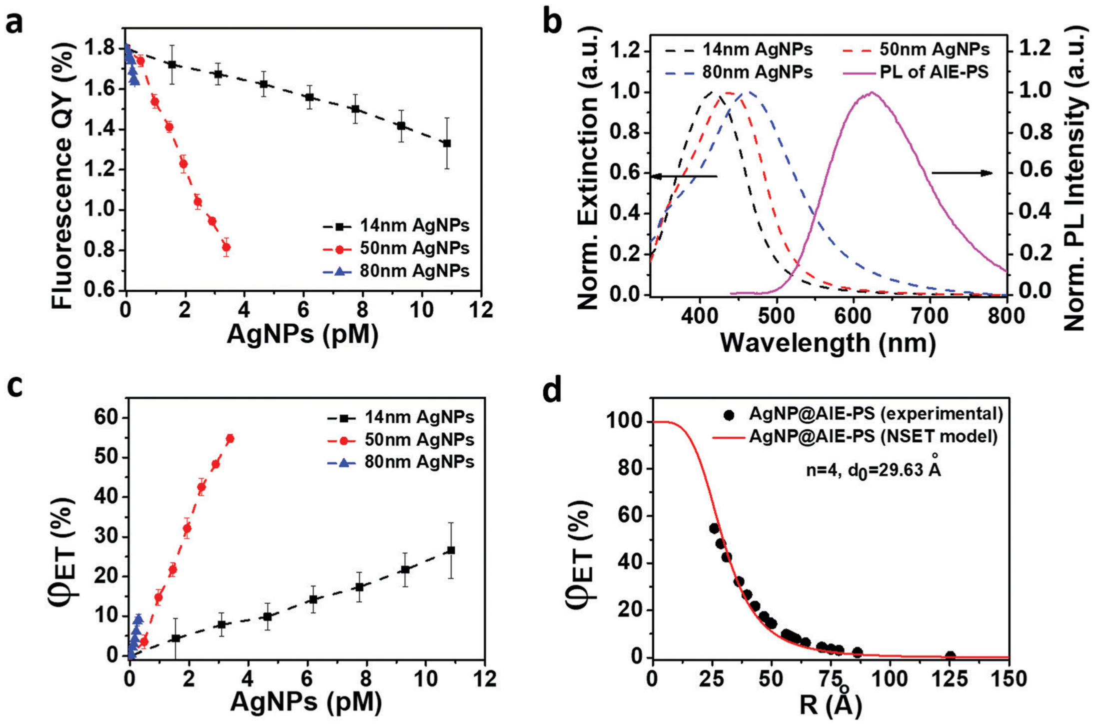

Fig. 3 (a) Change (%) in the fluorescence quantum yield (QY) of different AgNP@AIE-PS samples, (b) spectral overlap between the extinction of AgNPs (dashed-dot lines, left axis) and emission of the AIE-PS (solid line, right axis), (c) energy transfer efficiency (ϕ_{ET} %) from the AIE-PS to the AgNPs as a function of the size and concentration of the AgNPs, and (d) fitting of experimental energy transfer data (black circles) with the nanometal surface energy transfer (NSET) model (red line) of AgNP@AIE-PS.

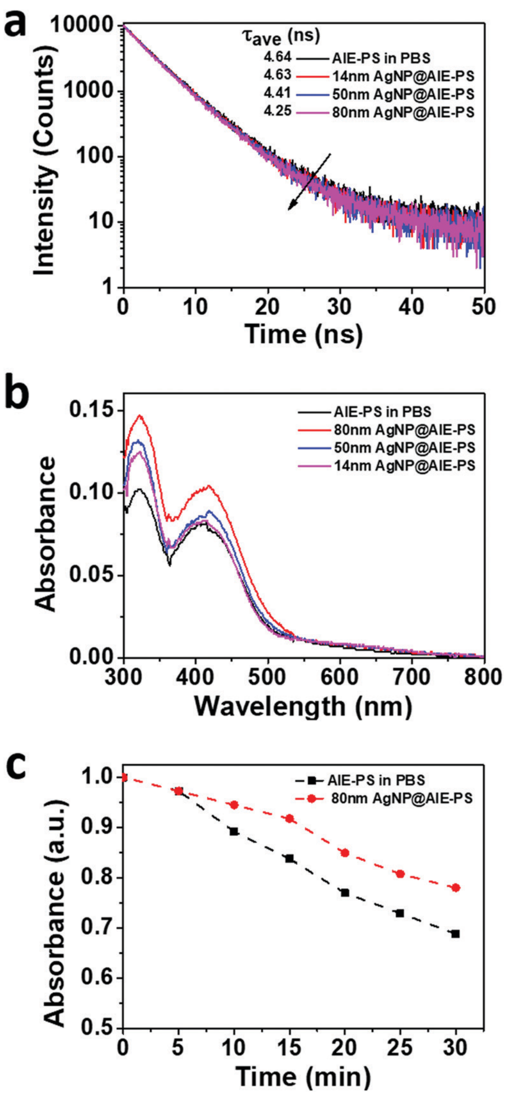

Fig. 4 (a) Fluorescence decay profile of the respective AgNP@AIE-PS hybrids with maximum ME-SOG. (b) Change in the absorbance spectra of the AIE-PS in PBS after forming a hybrid with AgNPs of different sizes. The absorbance of the AgNPs has been subtracted from the spectra. (c) Comparison of the photostability between 80 nm AgNP@AIE-PS and the AIE-PS alone in PBS buffer. Both samples were irradiated with 100 mW cm^{-2} white light. All the samples were prepared at a concentration of 3 pM 14 nm AgNPs, 2 pM 50 nm AgNPs, 0.22 pM 80 nm AgNPs, and 9 μM of AIE-PS molecules, respectively. The excitation and emission wavelengths for the fluorescence measurements are λ_{ex} = 374 nm and λ_{em} = 625 nm, respectively.

showing its great promise as a theranostic agent for long-time PDT and cell tracking.

As depicted in the simplified Jablonski diagram in Scheme 1, the excited electrons come back to the ground state *via* radiative (fluorescence) or non-radiative decay, while some of them can go to the triplet state *via* the intersystem crossing (ISC) process. The electrons in the triplet state can produce singlet oxygen molecules ($^1O_2$) *via* energy transfer to the surrounding triplet molecular oxygen ($^3O_2$). In the presence of AgNPs (Scheme 1b), their strong light scattering provides more photons to be absorbed by the AIE-PS. Therefore, the excitation rate in the AIE-PS is increased due to the enhanced photon absorption as well as the enhanced electric field around the AgNPs. The higher rate for excitation of electrons in the singlet state leads to an increase in the ISC rate. This would result in a larger number of electrons present in the triplet state, causing more singlet oxygen to be generated. However, there is substantial energy transfer from the excited AIE-PS* molecules to the surface of AgNPs *via* the NSET mechanism, which neutralizes the effect of enhanced excitation by the AgNPs. This explains why there is only slight fluorescence quenching (5% for 0.22 pM 80 nm AgNPs) observed in the 80 nm AgNP@AIE-PS with the highest SOG enhancement effect in the nanohybrid system.

2.3. Cytotoxicity and application of AgNP@AIE-PS for fluorescence imaging and cancer cell ablation

Firstly, the cytotoxicity of the 80 nm AgNP@AIE-PS was evaluated using the MTT viability assay on both NIH-3T3 mammalian cells and HeLa cancer cells. Three control samples including (1) 80 nm AgNPs, (2) the AIE-PS and (3) SNP@AIE-PS prepared using the same concentration of AIE-PS were also subjected to the cell viability test (Fig. S5, ESI†). The results show that the AIE-PS possesses good cytotoxicity (*i.e.*, cell viability >85% at a concentration <10 μM), while the presence of AgNPs causes a slight drop (~5%) in the cell viability as compared with the SNP@AIE-PS control sample. Cellular imaging experiments were carried out upon incubating the 80 nm AgNP@AIE-PS with HeLa cells for 12 h prior to the cellular imaging experiments. A similar experiment was done using SNP@AIE-PS and the AIE-PS alone in PBS as controls. Surprisingly, the fluorescence image of HeLa cells in the presence of AgNP@AIE-PS (Fig. 5a) was much brighter than that with the AIE-PS alone in PBS (Fig. 5b), while a similar brightness was observed in the SNP@AIE-PS control sample (Fig. 5c). As the the fluorescence intensities of the three tested samples are similar (prior to the cellular experiments), the observed brighter cellular images could be due to the difference in the overall size of each sample (*i.e.*, ~80 nm AgNP@AIE-PS, 104 nm SNP@AIE-PS, and 160 nm AIE-PS aggregates in PBS[43]), leading to differential uptake efficiency by the HeLa cells. Therefore, lower cellular uptake for AIE-PS aggregates alone in PBS was observed as compared to the 80nm AgNP@AIE-PS sample.[52,53] Next, the *in vitro* photodynamic efficiency of the 80 nm AgNP@AIE-PS was evaluated by treating HeLa cells under white light with a power of 40 mW cm^{-2}. Fig. 5d shows the cell viability in the presence of 80 nm AgNP@AIE-PS after treating with white light for 10 minutes. The results show that the PDT treatment with 80 nm AgNP@AIE-PS can effectively kill the cancer cells (~85% cell death, 10 μM AIE-PS) within 10 min, the performance of which is better than that using the AIE-PS alone (20% cell death) as well as the control sample (23% cell death) tested under the same conditions. This results shows the promising use of the AgNP-enhanced AIE-PS as a next-generation biocompatible photo-theranostic agent for simultaneous bioimaging and effective photodynamic therapy.

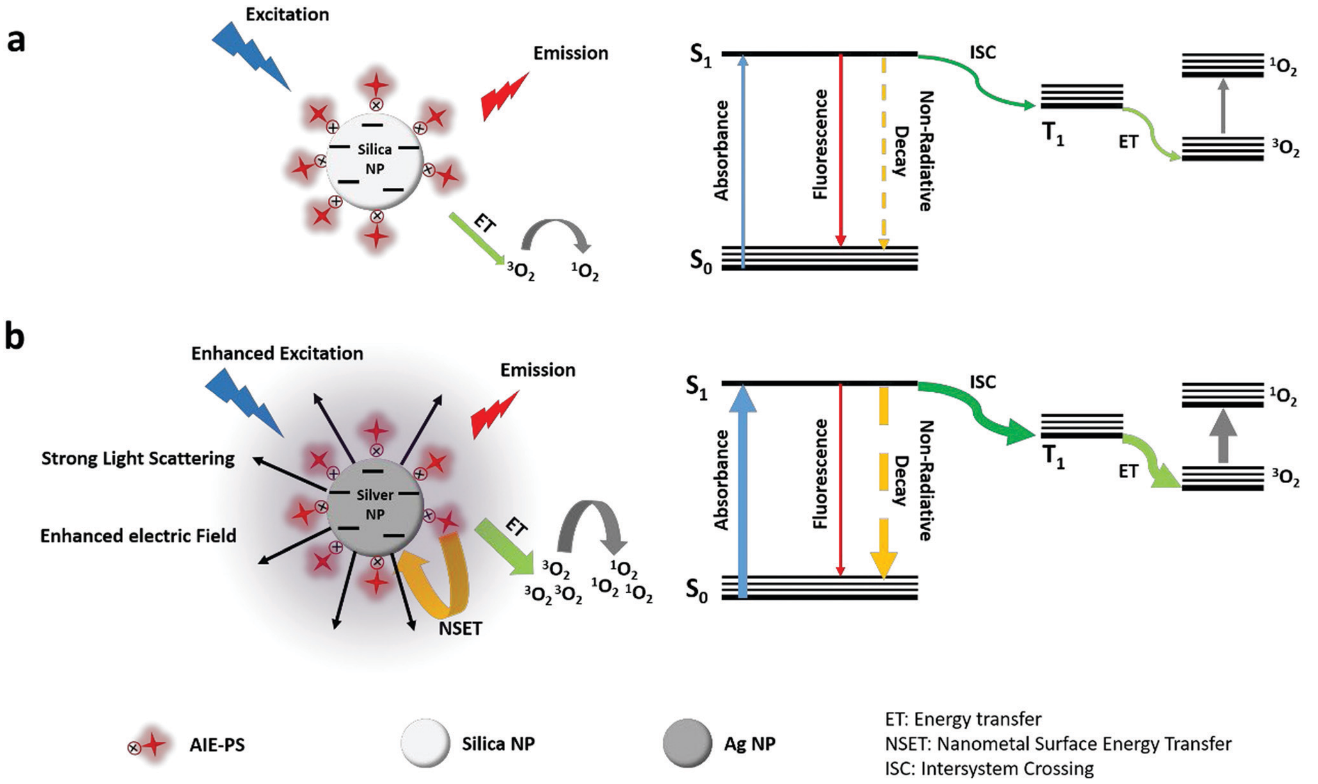

Scheme 1 Simplified Jablonski diagram for the (a) SNP@AIE-PS hybrid and (b) Ag@AIE-PS hybrid. ET is the energy transfer from the excited AIE-PS (in the triplet state) to the surrounding oxygen molecules. ISC stands for the intersystem crossing process ($S_1 \rightarrow T_1$). The thicker arrows refer to an enhanced rate in each process. In part (b), the purple glow and black arrows around the silver nanoparticle refer to the enhanced electric field around the AgNP and strong light scattering by the AgNP, respectively.

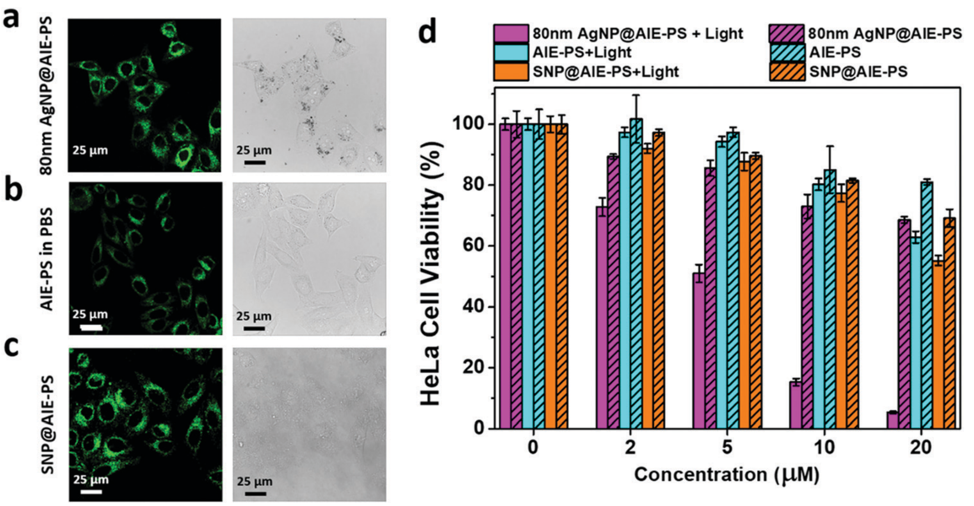

Fig. 5 CLSM (left) and bright-field (right) images of HeLa cells incubated with 10 μM of (a) 80 nm AgNP@AIE-PS, (b) the AIE-PS in PBS, and (c) SNP@AIE-PS; (d) *in vitro* photodynamic therapy of HeLa cells treated with 80 nm AgNP@AIE-PS (cyan) and SNP@AIE-PS (violet) under white light irradiation (40 mW cm^{-2}) for 10 minutes. Control studies showing cell viability in the presence of respective samples under dark conditions (pattern-filled).

3. Conclusions

In summary, a unique theranostic photosentizer comprising silver nanoparticles (AgNPs) and an AIE luminogen has been developed for simultaneous cellular imaging and photodynamic therapy (PDT). AgNP@AIE-PS was formed *via* a simple electrostatic-induced aggregation approach. It was found that the size and concentration of AgNPs were critical in dictating the metal-enhanced singlet oxygen generation (ME-SOG) property of the nanohybrids. Typically, larger AgNPs can lead to higher SOG enhancement at a lower AgNP concentration, among which the 80 nm AgNP@AIE-PS could achieve a 10-fold enhancement of the SOG capability compared to the AIE-PS alone. Simulation studies have been conducted to confirm that the enhanced singlet oxygen generation in AgNP@AIE-PS was due to the excellent scattering efficiency of metal NPs and electric field enhanced plasmonic coupling effect in the resulting hybrids. It is noteworthy that only minimum fluorescence quenching (5%) with a slight decrease in fluorescence lifetime was observed for the 80 nm AgNP@AIE-PS hybrid. Thus, it is bright enough to be used for simultaneous cellular imaging and photodynamic therapy. In summary, the as-developed AgNP@AIE-PS possesses many unique features, including ME-SOG, high fluorescent brightness, good photostability and low cytotoxicity, making it a promising next-generation multifunctional photosensitizer for theranostic applications.

4. Experimental section

4.1. Materials

Chemicals including silver nitrate, tannic acid (TA), 4-mercaptobenzoic acid (4-MBA), potassium carbonate (K_2CO_3), 9,10-anthracenediyl-bis(methylene)dimalonic acid (ABDA), Rose Bengal, 4-(dicyanomethylene)-2-methyl-6-(*p*-dimethylaminostyryl)-4*H*-pyran (DCM), ethanol, tetraethyl orthosilicate (TEOS), ammonia solution (25%), and phosphate buffer solution (PBS, 1×) were purchased from Sigma–Aldrich and used as received. Ultrapure water (18.2 MΩ cm) was used to prepare all aqueous solutions.

4.2. Synthesis of the water-soluble red-emissive AIE-based photosensitizer

The red-emissive AIE photosensitizer was synthesized according to a previous report.[43]

4.3. Synthesis of silica nanoparticles

The silica nanoparticles were synthesized according to the modified Stöber method reported in the literature.[54,55] Briefly, a mixture of water (8.83 mL), ammonia solution (1 mL), and ethanol (5.67 mL) was prepared. Then, TEOS (1.35 mL) was dissolved in ethanol (13.65 mL) and added to the prepared solution dropwise with vigorous stirring. After 30 min at room temperature, the nanoparticles were washed with ethanol and water to remove unreacted chemicals. Finally, the obtained nanoparticles were dispersed in deionized water (25 mL) by 30 min bath ultrasonication. The final concentration of silica nanoparticles was 1.67 nM.[33]

4.4. Synthesis of 4-mercaptobenzoic acid-capped AgNPs

4-Mercaptobenzoic acid-capped AgNPs (4-MBA-AgNPs) were synthesized by a ligand exchange approach.[56] First, tannic acid-capped AgNPs (TA-AgNPs) were synthesized according to the literature.[57] Tannic acid was used as both the reducing and capping agent. Briefly, a tannic acid solution (500 μL, 5 mM) was added to deionized water (DI-water, 19 mL). Then, the solution pH was adjusted to 8, 6.5 and 6 with K_2CO_3 solution (0.05 M). Finally, $AgNO_3$ (500 μL, 100 mM) was added to the above mixture under constant stirring. AgNPs of 14 nm and 50 nm were collected after 2 h of reaction and 80 nm AgNPs were collected after 6 h of reaction. The as-synthesized AgNPs were dialyzed against DI-water for 24 h prior to ligand exchange. To make 4-mercaptobenzoic acid-capped AgNPs, TA-AgNPs (20 mL) were transferred to a round-bottom flask, followed by addition of 4-MBA (2 mL, 1 mM in 0.1 M NaOH). The mixture solution was stirred vigorously for 2 h to complete the reaction. The final solution was collected and dialyzed against 0.01 M NaOH solution overnight. The concentrations of AgNPs in the final products were estimated to be 155 pM, 48.3 pM, and 4.23 pM for the 14 nm, 50 nm and 80 nm AgNP samples, respectively, according to the extinction molar coefficients reported in the literature.[58]

4.5. Preparation of AgNP@AIE-PS nanohybrids with maximum SOG enhancement

AgNP@AIE-PS nanohybrids with different sizes of the Ag core (*i.e.*, 14 nm, 50 nm, and 80 nm) were prepared by the adsorption of positively-charged AIE-PS molecules onto the surface of negatively-charged 4-MBA-capped AgNPs. Briefly, an AIE-PS solution in DMSO (*i.e.*, a final concentration of 9 μM) was mixed with the respective size AgNPs under different optimized conditions (*i.e.*, 3 pM for 14 nm AgNPs, 2 pM for 50 nm AgNPs, and 0.22 pM for 80 nm AgNPs) to form the AgNP@AIE-PS nanohybrids with maximum SOG enhancement. The pH was set at 4 to maximize the electrostatic interactions between the AIE-PS molecules and AgNPs. The mixture was stirred for 20 min to complete the adsorption process.

4.6. Characterization

Fluorescence and UV-visible absorption spectra were recorded using an Infinite M-200 microplate reader and Shimadzu UV-2450 spectrophotometer, respectively. TEM images were obtained on a JEOL JEM-2010F transmission electron microscope operating at 200 kV. The zeta potential and hydraulic size of the samples were acquired on a Malvern Zetasizer at room temperature.

4.7. Fluorescence quantum yield measurements

The fluorescence quantum yield (QY) of the samples was measured using DCM as a reference in water. The quantum yield was calculated according to the following formula:

$$\mathrm{QY} = \mathrm{QY}_{\mathrm{Ref}} \times \frac{F}{F_{\mathrm{Ref}}} \times \frac{A_{\mathrm{Ref}}}{A} \times \frac{n^2}{{n_{\mathrm{Ref}}}^2} \tag{3}$$

where QY and $\mathrm{QY_{Ref}}$ are the fluorescence quantum yields of the sample and reference, respectively. F and F_{ref} are the integral of the fluorescence spectra of the sample and reference in the range of 400 nm to 800 nm, respectively. A and A_{Ref} refer to the absorbance of the sample and reference at the excitation wavelength (400 nm).

4.8. Detection of singlet oxygen ($^1O_2$) generation

The singlet oxygen generation rate was measured using ABDA as an indicator. The AgNP@AIE-PS hybrid (1 mL, with a final

AIE-PS concentration of 9 μM) was transferred to a disposable cuvette (1 mL). The sample was irradiated with 40 mW cm^{-2} white light in the presence of ABDA (a final concentration of 50 μM). The absorbance of the sample was measured every 10 min, and the rate of ABDA degradation was calculated using the following first-order kinetic model:[59]

$$\ln\left(\frac{A(t)}{A(0)}\right) = -K \cdot t \tag{4}$$

where $A(t)$ and $A(0)$ are the absorbance of ABDA at 379 nm at time t and 0, respectively. K is the first-order kinetic constant for degradation of ABDA and t is time. The absorbance of each photosensitizer sample was subtracted from the observed absorbance of ABDA before calculation of the degradation rate.

4.9. $^1O_2$ quantum yield measurements

The $^1O_2$ quantum yield was measured by a chemical trapping method using ABDA as a $^1O_2$ selective indicator. Water-soluble Rose Bengal was selected as a reference photosensitizer. Briefly, an aqueous solution (1 mL) containing AgNP@AIE-PS or Rose Bengal (5 μM) and 50 μM ABDA was prepared and subjected to white light irradiation at the same conditions as aforementioned. The degradation rate of ABDA was monitored by measuring its absorbance intensity at 379 nm under irradiation over time. The $^1O_2$ quantum yield was calculated using the following equation:

$$\varphi = \varphi_{\mathrm{RB}} \times \frac{K}{K_{\mathrm{RB}}} \times \frac{A_{\mathrm{RB}}}{A} \tag{5}$$

where K and K_{RB} are the degradation rate of ABDA by the test sample and Rose Bengal, respectively. A and A_{RB} are the integral of the absorbance spectra data for the sample and Rose Bengal in the wavelength range of 400–800 nm. φ_{RB} is the $^1O_2$ quantum yield of Rose Bengal in water, which is 75%.

4.10. Time-resolved fluorescence spectroscopy

The as-prepared AgNP@AIE-PS samples were excited at 374 nm using a FluoTime 200 TCSPC machine (Picoquant BmbH, Germany) for fluorescent lifetime measurements. The fluorescence decay profile of the samples was collected at 625 nm and modeled using the two-exponential equation below:

$$I(t) = \sum \alpha_i \exp(-t/\tau_i) \tag{6}$$

where $I(t)$ is the fluorescence intensity at time t, τ_i is the decay time, α_i is the amplitude, and $\sum \alpha_i = 1$. The average life-time can be written as:

$$\bar{\tau} = \sum f_i \tau_i \tag{7}$$

where the contribution fraction of each component (f_i) is given as follows:

$$f_i = \frac{\alpha_i \tau_i}{\sum \alpha_i \tau_i} \tag{8}$$

The curve fitting was performed using the curve-fitting toolbox in Matlab 2014b software.

4.11. Cell culture

HeLa cells and NIH-3T3 cells were pre-cultured in Dulbecco's Modified Eagle Medium (DMEM) with 10% Fetal Bovine Serum (FBS) and 1% penicillin–streptomycin at 37 °C in a humidified incubator containing 5% CO_2.

4.12. Cellular imaging

After reaching confluence, pre-cultured cells were seeded in 8-well chambered cover glass (Nunc Lab-Tek, Thermo Scientific). After adherence, fresh DMEM containing the AIE-PS or 80 nm AgNP@AIE-PS was added and incubated for 12 h at 10 μM (based on the AIE-PS). FBS-free DMEM was used during CLSM imaging. Cell images were taken using a Leica SP8X laser scanning confocal microscope.

4.13. Cytotoxicity study

Methylthiazolyldiphenyltetrazolium bromide (MTT) assay was used to evaluate the cytotoxicity of the AgNP@AIE-PS hybrid system. For the dark cytotoxicity, pre-cultured cells were seeded into 96-well plates at a density of 4000 cells per well. After reaching confluence, fresh DMEM containing the AIE-PS and 80 nm AgNP@AIE-PS was added and incubated for 24 hours at different concentrations. The medium was replaced by 0.5 mg mL^{-1} methylthiazolyldiphenyltetrazolium bromide in the medium for 4 hours, and DMSO was used to dissolve non-soluble formazan. The absorbance was measured by a microplate reader at 570 nm. For the photodynamic therapy (PDT) study, cells were treated for the same time period at the same concentrations. After changing to fresh medium, 10 min white light irradiation at 40 mW cm^{-2} was applied to the cells, and the treated cells were further cultured for 6 hours. Standard MTT assay was performed after the PDT study to evaluate the light treatment efficiency. Each condition was repeated three times to calculate the standard deviation.

4.14. Simulation study

In order to calculate the electric field and scattering cross-section of spherical AgNPs, finite element method (FEM) simulations were carried out in the COMSOL multiphysics software package (see www.comsol.com). The complex refractive index of Ag was taken from the CRC handbook.[60] Water was used as the surrounding environment. A plane wave propagating in the x-direction and linearly polarized along the z-axis spanning the wavelength range of 300 nm to 700 nm was set as the source. Due to the symmetry of the problem, only one-quarter of the sphere was modeled.

Conflicts of interest

There are no conflicts to declare.

Acknowledgements

M. T. Y. would like to thank Dr Soroosh Daqiqeh Rezaei for his valuable help and discussion on the simulation part. M. T. Y.

also would like to thank the Agency of Science, Technology and Research, Singapore (A*STAR) for financial support *via* the SINGA scholarship. This work was supported by the Institute of Materials Research and Engineering, A*STAR, under Biomimetic and Biomedical Materials program (IMRE/00-1P1400), in collaboration with Newcastle University (RSA/CCEAMD5010), UK and Singapore. The financial support from National University of Singapore (R279-000-482-133) and National Research Foundation (R279-000-444-281) is also appreciated.

References

1 A. Gupta, S. Wang, P. Pera, K. Rao, N. Patel, T. Y. Ohulchanskyy, J. Missert, J. Morgan, Y.-E. Koo-Lee and R. Kopelman, Multifunctional nanoplatforms for fluorescence imaging and photodynamic therapy developed by post-loading photosensitizer and fluorophore to polyacrylamide nanoparticles, *J. Nanomed. Nanotechnol.*, 2012, **8**, 941–950.

2 J. P. Celli, B. Q. Spring, I. Rizvi, C. L. Evans, K. S. Samkoe, S. Verma, B. W. Pogue and T. Hasan, Imaging and photodynamic therapy: mechanisms, monitoring, and optimization, *Chem. Rev.*, 2010, **110**, 2795–2838.

3 J. F. Lovell, T. W. Liu, J. Chen and G. Zheng, Activatable photosensitizers for imaging and therapy, *Chem. Rev.*, 2010, **110**, 2839–2857.

4 Y. Yu, W. D. Lee and Y. N. Tan, Protein-protected gold/silver alloy nanoclusters in metal-enhanced singlet oxygen generation and their correlation with photoluminescence, *Mater. Sci. Eng., C*, 2020, **109**, 110525.

5 X. T. Zheng, Y. C. Lai and Y. N. Tan, Nucleotide-derived theranostic nanodots with intrinsic fluorescence and singlet oxygen generation for bioimaging and photodynamic therapy, *Nanoscale Adv.*, 2019, **1**, 2250–2257.

6 Y. Yu, J. Geng, E. Y. X. Ong, V. Chellappan and Y. N. Tan, Bovine Serum Albulmin Protein-Templated Silver Nanocluster (BSA-Ag13): An Effective Singlet Oxygen Generator for Photodynamic Cancer Therapy, *Adv. Healthcare Mater.*, 2016, **5**, 2528–2535.

7 Y. Choi, X. T. Zheng and Y. N. Tan, Bioinspired carbon dots (biodots): emerging fluorophores with tailored multiple functionalities for biomedical, agricultural and environmental applications, *Mol. Syst. Des. Eng.*, 2020, **5**, 67–90.

8 T. J. Dougherty, C. J. Gomer, B. W. Henderson, G. Jori, D. Kessel, M. Korbelik, J. Moan and Q. Peng, Photodynamic therapy, *J. Natl. Cancer Inst.*, 1998, **90**, 889–905.

9 E. S. Marmur, C. D. Schmults and D. J. Goldberg, A review of laser and photodynamic therapy for the treatment of nonmelanoma skin cancer, *Dermatol. Surg.*, 2004, **30**, 264–271.

10 J. Fuchs and J. Thiele, The role of oxygen in cutaneous photodynamic therapy, *Free Radical Biol. Med.*, 1998, **24**, 835–847.

11 M. A. Doustvandi, F. Mohammadnejad, B. Mansoori, H. Tajalli, A. Mohammadi, A. Mokhtarzadeh, E. Baghbani, V. Khaze, K. Hajiasgharzadeh, M. M. Moghaddam, M. R. Hamblin and B. Baradaran, Photodynamic therapy using zinc phthalocyanine with low dose of diode laser combined with doxorubicin is a synergistic combination therapy for human SK-MEL-3 melanoma cells, *Photodiagn. Photodyn. Ther.*, 2019, **28**, 88–97.

12 L. B. Negri, T. J. Martins, R. S. da Silva and M. R. Hamblin, Photobiomodulation combined with photodynamic therapy using ruthenium phthalocyanine complexes in A375 melanoma cells: Effects of nitric oxide generation and ATP production, *J. Photochem. Photobiol., B*, 2019, **198**, 111564.

13 Z. Zhou, J. Song, L. Nie and X. Chen, Reactive oxygen species generating systems meeting challenges of photodynamic cancer therapy, *Chem. Soc. Rev.*, 2016, **45**, 6597–6626.

14 L. Huang, B. Bhayana, W. Xuan, R. P. Sanchez, B. J. McCulloch, S. Lalwani and M. R. Hamblin, Comparison of two functionalized fullerenes for antimicrobial photodynamic inactivation: Potentiation by potassium iodide and photochemical mechanisms, *J. Photochem. Photobiol., B*, 2018, **186**, 197–206.

15 W. Xuan, Y. He, L. Huang, Y.-Y. Huang, B. Bhayana, L. Xi, J. A. Gelfand and M. R. Hamblin, Antimicrobial Photodynamic Inactivation Mediated by Tetracyclines in Vitro and in Vivo: Photochemical Mechanisms and Potentiation by Potassium Iodide, *Sci. Rep.*, 2018, **8**, 17130.

16 J. B. Birks, *Photophysics of aromatic molecules*, 1970.

17 C. Tanielian, C. Wolff and M. Esch, Singlet oxygen production in water: aggregation and charge-transfer effects, *J. Phys. Chem.*, 1996, **100**, 6555–6560.

18 J. F. Lovell, C. S. Jin, E. Huynh, H. Jin, C. Kim, J. L. Rubinstein, W. C. Chan, W. Cao, L. V. Wang and G. Zheng, Porphysome nanovesicles generated by porphyrin bilayers for use as multimodal biophotonic contrast agents, *Nat. Mater.*, 2011, **10**, 324.

19 J. F. Lovell, J. Chen, M. T. Jarvi, W.-G. Cao, A. D. Allen, Y. Liu, T. T. Tidwell, B. C. Wilson and G. Zheng, FRET quenching of photosensitizer singlet oxygen generation, *J. Phys. Chem. B*, 2009, **113**, 3203–3211.

20 F. Hu, D. Mao, Y. Wang, W. Wu, D. Zhao, D. Kong and B. Liu, Metal–Organic Framework as a Simple and General Inert Nanocarrier for Photosensitizers to Implement Activatable Photodynamic Therapy, *Adv. Funct. Mater.*, 2018, **28**, 1707519.

21 W. Wu, D. Mao, F. Hu, S. Xu, C. Chen, C. J. Zhang, X. Cheng, Y. Yuan, D. Ding and D. Kong, A Highly Efficient and Photostable Photosensitizer with Near-Infrared Aggregation-Induced Emission for Image-Guided Photodynamic Anticancer Therapy, *Adv. Mater.*, 2017, **29**, 1700548.

22 F. Hu, S. Xu and B. Liu, Photosensitizers with Aggregation-Induced Emission: Materials and Biomedical Applications, *Adv. Mater.*, 2018, **30**, 1801350.

23 J. Geng, W. L. Goh, C. Zhang, D. P. Lane, B. Liu, F. Ghadessy and Y. N. Tan, A highly sensitive fluorescent light-up probe for real-time detection of the endogenous protein target and its antagonism in live cells, *J. Mater. Chem. B*, 2015, **3**, 5933–5937.

24 F. Hu, Y. Yuan, W. Wu, D. Mao and B. Liu, Dual-Responsive Metabolic Precursor and Light-Up AIEgen for Cancer Cell

Bio-orthogonal Labeling and Precise Ablation, *Anal. Chem.*, 2018, **90**, 6718–6724.

25 F. Hu, D. Mao, X. Cai, W. Wu, D. Kong and B. Liu, A Light-Up Probe with Aggregation-Induced Emission for Real-Time Bio-orthogonal Tumor Labeling and Image-Guided Photodynamic Therapy, *Angew. Chem.*, 2018, **130**, 10339–10343.

26 F. Hu, S. Xu and B. Liu, Photosensitizers with Aggregation-Induced Emission: Materials and Biomedical Applications, *Adv. Mater.*, 2018, 1801350.

27 J. Ferreira, P. F. Menezes, C. Kurachi, C. Sibata, R. Allison and V. S. Bagnato, Photostability of different chlorine photosensitizers, *Laser Phys. Lett.*, 2007, **5**, 156.

28 Y. Zhang, K. Aslan, M. J. Previte and C. D. Geddes, Metal-enhanced singlet oxygen generation: a consequence of plasmon enhanced triplet yields, *J. Fluoresc.*, 2007, **17**, 345–349.

29 Y. Zhang, K. Aslan, M. J. Previte and C. D. Geddes, Plasmonic engineering of singlet oxygen generation, *Proc. Natl. Acad. Sci. U. S. A.*, 2008, **105**, 1798–1802.

30 C. D. Geddes and J. R. Lakowicz, Metal-enhanced fluorescence, *J. Fluoresc.*, 2002, **12**, 121–129.

31 K. Aslan, I. Gryczynski, J. Malicka, E. Matveeva, J. R. Lakowicz and C. D. Geddes, Metal-enhanced fluorescence: an emerging tool in biotechnology, *Curr. Opin. Biotechnol*, 2005, **16**, 55–62.

32 J. R. Lakowicz, Radiative decay engineering 5: metal-enhanced fluorescence and plasmon emission, *Anal. Biochem.*, 2005, **337**, 171–194.

33 S. Dinda, F. L. Yap, V. Suresh, R. K. Gupta, D. Das and S. Krishnamoorthy, Quantitative Detection with Surface Enhanced Raman Scattering (SERS) Using Self-Assembled Gold Nanoparticle Cluster Arrays, *Aust. J. Chem.*, 2013, **66**, 1034–1038.

34 M. Tavakkoli Yaraki, S. Daqiqeh Rezaei and Y. N. Tan, Simulation guided design of silver nanostructures for plasmon-enhanced fluorescence, singlet oxygen generation and SERS applications, *Phys. Chem. Chem. Phys.*, 2020, **22**, 5673–5687.

35 M. Tavakkoli Yaraki, S. Daqiqeh Rezaei, E. Middha and Y. N. Tan, Synthesis and Simulation Study of Right Silver Bipyramids via Seed-Mediated Growth cum Selective Oxidative Etching Approach, *Part. Part. Syst. Charact.*, 2020, **37**, 2000027.

36 M. K. Khaing Oo, Y. Yang, Y. Hu, M. Gomez, H. Du and H. Wang, Gold nanoparticle-enhanced and size-dependent generation of reactive oxygen species from protoporphyrin IX, *ACS Nano*, 2012, **6**, 1939–1947.

37 M. Tavakkoli Yaraki, F. Hu, S. Daqiqeh Rezaei, B. Liu and Y. N. Tan, Metal-enhancement study of dual functional photosensitizers with aggregation-induced emission and singlet oxygen generation, *Nanoscale Adv.*, 2020, **2**, 2859–2869.

38 N. Macia, R. Bresoli-Obach, S. Nonell and B. Heyne, Hybrid Silver Nanocubes for Improved Plasmon-Enhanced Singlet Oxygen Production and Inactivation of Bacteria, *J. Am. Chem. Soc.*, 2018, **141**, 684–692.

39 O. Planas, N. Macia, M. Agut, S. Nonell and B. Heyne, Distance-dependent plasmon-enhanced singlet oxygen production and emission for bacterial inactivation, *J. Am. Chem. Soc.*, 2016, **138**, 2762–2768.

40 Y. Cheng, A. C. Samia, J. D. Meyers, I. Panagopoulos, B. Fei and C. Burda, Highly efficient drug delivery with gold nanoparticle vectors for in vivo photodynamic therapy of cancer, *J. Am. Chem. Soc.*, 2008, **130**, 10643–10647.

41 N. L. Pacioni, M. a. González-Béjar, E. Alarcón, K. L. McGilvray and J. Scaiano, Surface plasmons control the dynamics of excited triplet states in the presence of gold nanoparticles, *J. Am. Chem. Soc.*, 2010, **132**, 6298–6299.

42 M. A. B. N. Rivas Aiello, J. J. Romero, S. G. Bertolotti, M. N. C. Gonzalez and D. O. Mártire, Effect of Silver Nanoparticles on the Photophysics of Riboflavin: Consequences on the ROS Generation, *J. Phys. Chem. C*, 2016, **120**, 21967–21975.

43 F. Hu, X. Cai, P. N. Manghnani, W. Wu and B. Liu, Multicolor monitoring of cellular organelles by single wavelength excitation to visualize the mitophagy process, *Chem. Sci.*, 2018, **9**, 2756–2761.

44 S. Xu, Y. Yuan, X. Cai, C.-J. Zhang, F. Hu, J. Liang, G. Zhang, D. Zhang and B. Liu, Tuning the singlet-triplet energy gap: a unique approach to efficient photosensitizers with aggregation-induced emission (AIE) characteristics, *Chem. Sci.*, 2015, **6**, 5824–5830.

45 Y. Chen, K. Munechika and D. S. Ginger, Dependence of Fluorescence Intensity on the Spectral Overlap between Fluorophores and Plasmon Resonant Single Silver Nanoparticles, *Nano Lett.*, 2007, **7**, 690–696.

46 J. John, L. Thomas, N. A. George, A. Kurian and S. D. George, Tailoring of optical properties of fluorescein using green synthesized gold nanoparticles, *Phys. Chem. Chem. Phys.*, 2015, **17**, 15813–15821.

47 D. Ghosh, A. Girigoswami and N. Chattopadhyay, Superquenching of coumarin 153 by gold nanoparticles, *J. Photochem. Photobiol., A*, 2012, **242**, 44–50.

48 V. May and O. Kühn, *Charge and energy transfer dynamics in molecular systems*, John Wiley & Sons, 2008.

49 R. Chance, A. Prock and R. Silbey, Molecular fluorescence and energy transfer near interfaces, *Adv. Chem. Phys.*, 1978, **37**, 1–65.

50 C. Yun, A. Javier, T. Jennings, M. Fisher, S. Hira, S. Peterson, B. Hopkins, N. Reich and G. Strouse, Nanometal surface energy transfer in optical rulers, breaking the FRET barrier, *J. Am. Chem. Soc.*, 2005, **127**, 3115–3119.

51 P. Pompa, L. Martiradonna, A. Della Torre, F. Della Sala, L. Manna, M. De Vittorio, F. Calabi, R. Cingolani and R. Rinaldi, Metal-enhanced fluorescence of colloidal nanocrystals with nanoscale control, *Nat. Nanotechnol.*, 2006, **1**, 126.

52 X.-Y. Sun, Q.-Z. Gan and J.-M. Ouyang, Size-dependent cellular uptake mechanism and cytotoxicity toward calcium oxalate on Vero cells, *Sci. Rep.*, 2017, **7**, 41949.

53 E. Oh, J. B. Delehanty, K. E. Sapsford, K. Susumu, R. Goswami, J. B. Blanco-Canosa, P. E. Dawson, J. Granek, M. Shoff, Q. Zhang, P. L. Goering, A. Huston and I. L. Medintz, Cellular Uptake and Fate of PEGylated Gold Nanoparticles Is Dependent on Both Cell-Penetration Peptides and Particle Size, *ACS Nano*, 2011, **5**, 6434–6448.

54 W. Stöber, A. Fink and E. Bohn, Controlled growth of monodisperse silica spheres in the micron size range, *J. Colloid Interface Sci.*, 1968, **26**, 62–69.

55 Y. Wang and B. Liu, Conjugated polyelectrolyte-sensitized fluorescent detection of thrombin in blood serum using aptamer-immobilized silica nanoparticles as the platform, *Langmuir*, 2009, **25**, 12787–12793.

56 J. V. Maya Girón, E. Zelaya, A. Rubert, G. Benítez, P. Carro, R. C. Salvarezza and M. E. Vela, Surface chemistry of 4-mercaptobenzoic acid self-assembled on Ag(111) and Ag nanoparticles, *J. Phys. Chem. C*, 2013, **117**, 24967–24974.

57 Y. Cao, R. Zheng, X. Ji, H. Liu, R. Xie and W. Yang, Syntheses and characterization of nearly monodispersed, size-tunable silver nanoparticles over a wide size range of 7–200 nm by tannic acid reduction, *Langmuir*, 2014, **30**, 3876–3882.

58 D. Paramelle, A. Sadovoy, S. Gorelik, P. Free, J. Hobley and D. G. Fernig, A rapid method to estimate the concentration of citrate capped silver nanoparticles from UV-visible light spectra, *Analyst*, 2014, **139**, 4855–4861.

59 N. A. Kuznetsova, N. S. Gretsova, O. A. Yuzhakova, V. M. Negrimovskii, O. L. Kaliya and E. A. Luk'yanets, New Reagents for Determination of the Quantum Efficiency of Singlet Oxygen Generation in Aqueous Media, *Russ. J. Gen. Chem.*, 2001, **71**, 36–41.

60 J. F. Shackelford, Y.-H. Han, S. Kim and S.-H. Kwon, *CRC materials science and engineering handbook*, CRC Press, 2016.